Title

Convex optimized diffusion encoding (CODE) gradient waveforms for minimum echo time and bulk motion–compensated diffusion-weighted MRI

Authors

Aliotta, Eric
Wu, Holden H
Ennis, Daniel B

Convex Optimized Diffusion Encoding (CODE) Gradient Waveforms for Minimum Echo Time and Bulk Motion–Compensated Diffusion-Weighted MRI

Eric Aliotta,[1,2] Holden H. Wu,[1,2] and Daniel B. Ennis[1,2]*

Purpose: To evaluate convex optimized diffusion encoding (CODE) gradient waveforms for minimum echo time and bulk motion–compensated diffusion-weighted imaging (DWI).
Methods: Diffusion-encoding gradient waveforms were designed for a range of b-values and spatial resolutions with and without motion compensation using the CODE framework. CODE, first moment (M_1) nulled CODE-M_1, and first and second moment (M_2) nulled CODE-M_1M_2 were used to acquire neuro, liver, and cardiac ADC maps in healthy subjects (n=10) that were compared respectively to monopolar (MONO), BIPOLAR ($M_1 = 0$), and motion-compensated (MOCO, $M_1 + M_2 = 0$) diffusion encoding.
Results: CODE significantly improved the SNR of neuro ADC maps compared with MONO (19.5 ± 2.5 versus 14.5 ± 1.9). CODE-M_1 liver ADCs were significantly lower (1.3 ± 0.1 versus $1.8 \pm 0.3 \times 10^{-3}$ mm^2/s, ie, less motion corrupted) and more spatially uniform (6% versus 55% ROI difference) than MONO and had higher SNR than BIPOLAR (SNR $= 14.9 \pm 5.3$ versus 8.0 ± 3.1). CODE-M_1M_2 cardiac ADCs were significantly lower than MONO (1.9 ± 0.6 versus 3.8 ± 0.3 x10^{-3} mm^2/s) throughout the cardiac cycle and had higher SNR than MOCO at systole (9.1 ± 3.9 versus 7.0 ± 2.6) while reporting similar ADCs (1.5 ± 0.2 versus $1.4 \pm 0.6 \times 10^{-3}$ mm^2/s).
Conclusions: CODE significantly improved SNR for ADC mapping in the brain, liver and heart, and significantly improved DWI bulk motion robustness in the liver and heart. **Magn Reson Med 77:717–729, 2017. © 2016 International Society for Magnetic Resonance in Medicine**

Key words:

INTRODUCTION

Diffusion-weighted imaging (DWI) is a powerful MRI technique that measures the self-diffusion of water in a wide variety of soft tissues to provide directionally dependent microstructural information. In the brain, DWI is used widely to estimate the apparent diffusion coefficient (ADC), and is the clinical gold standard for detection of acute and chronic stroke. DWI has also dem-onstrated clinical value in the heart (1–3) and liver (4–7), but sensitivity to cardiac and respiratory bulk motion frequently contributes to large signal losses that confound diffusion-weighted measurements in these regions (8–12).

DWI generally uses a spin-echo echo planar imaging (SE-EPI) sequence with large, motion-sensitizing, monopolar diffusion-encoding gradients. Consequently, any bulk motion that occurs during diffusion encoding leads to substantial signal losses and elevated ADC measurements. These errors cannot be corrected retrospectively, which means they must be prevented with prospective changes to the DWI sequence.

Synchronizing the DWI acquisition with physiologic motion is a frontline approach to mitigating bulk motion artifacts. In the liver, bulk motion artifacts can be largely eliminated by implementing cardiac and respiratory triggering (13–15), but this significantly increases acquisition durations. In the heart, cardiac triggering and respiratory motion compensation (through triggering, breath holds, or navigators) are insufficient to suppress bulk motion artifacts (9,11,12). Bulk motion sensitivity can be further reduced by shortening the temporal footprint of the diffusion-encoding gradient, as in DWI with stimulated echoes (16).

Implementing motion-compensated (MOCO) diffusion-encoding gradient waveforms with nulled first and/or second-order gradient moments (M_1, M_2) can mitigate sensitivity to bulk motion. For example, velocity-compensated diffusion-encoding gradient waveforms ($M_1 = 0$) have been implemented in the liver and demonstrate improved ADC measurement reproducibility without respiratory or cardiac triggering (17,18). Similarly, velocity and acceleration-compensated waveforms ($M_1 = M_2 = 0$) have been shown to improve dramatically the bulk motion robustness of cardiac DWI (19–21).

Conventional MOCO diffusion encoding is accomplished using a multipolar gradient waveform that necessarily and significantly increases the echo time (TE) compared with monopolar encoding, degrading SNR in the absence of bulk motion. Note, however, that the TE of SE-EPI DWI is dictated by the temporal footprint of (1) the diffusion-encoding gradient, and (2) the echo planar imaging (EPI) readout (from its start to the TE). Consequently, there is always dead time between the excitation and refocusing pulses (Figs. 1a, 1c, and 1e). This dead time increases with longer EPI readouts (eg, higher spatial resolution, lower bandwidth). In principle, this dead time can be filled with diffusion-encoding

[1]Department of Radiological Sciences, University of California, Los Angeles, California, USA.

[2]Biomedical Physics Interdepartmental Program, University of California, Los Angeles, California, USA.

*Correspondence to: Daniel B. Ennis, PhD, Peter V. Ueberroth Building, Suite 1471, Room B, 10945 Le Conte Avenue, Los Angeles, CA 90095. Telephone: 310.206.0713; Fax: 310.825.5837; E-mail: daniel.ennis@ucla.edu.
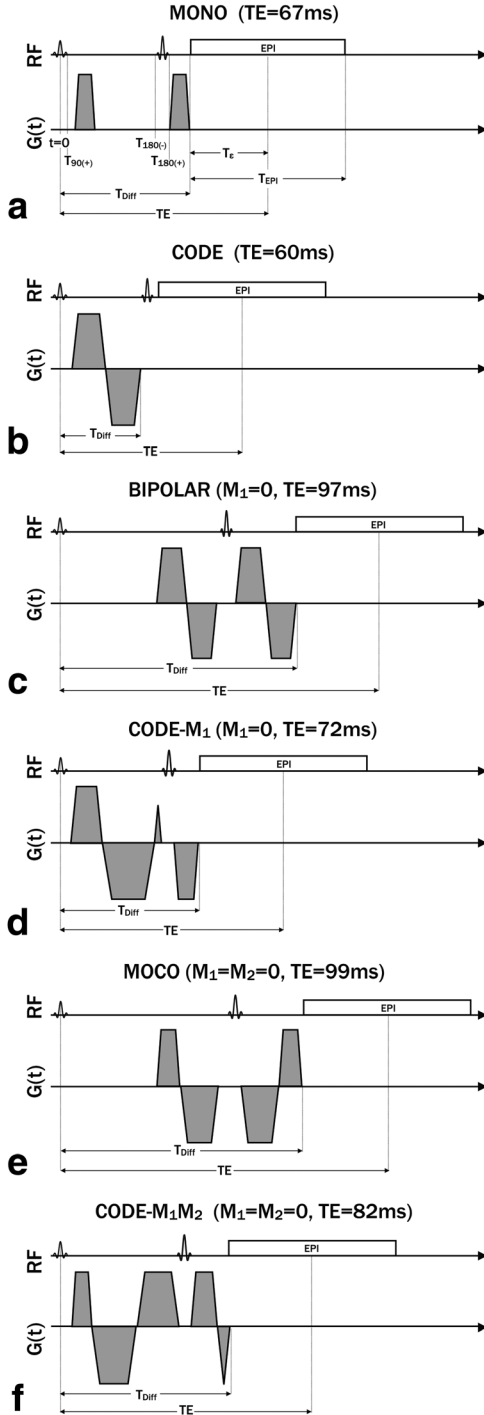
FIG. 1. Diffusion-encoding gradient waveforms for b = 500 s/mm^2 and T$_\varepsilon$ = 26.4 ms (2x2 mm spatial resolution with 300x300 mm FOV, 1740 Hz/px BW, and GRAPPA acceleration factor 2) with conventional monopolar (a), CODE optimized monopolar (b), conventional bipolar (velocity insensitive) (c), CODE-M$_1$ (d), conventional M$_1^+$M$_2$ nulled (velocity and acceleration insensitive) (d), and CODE-M$_1$M$_2$ encoding (f). CODE reduced the TE in all cases. Conventional encoding schemes (a, c, and e) all have dead time that the CODE framework uses to minimize the diffusion-encoding duration.

gradients, such that less diffusion encoding is needed after the refocusing pulse, consequently decreasing the TE.

In this study, we present a versatile optimization framework to redesign the diffusion-encoding gradient waveforms to be M$_1$ or M$_1$+M$_2$ compensated to mitigate the sensitivity to bulk motion artifacts and eliminate dead time. This approach significantly shortens the TE in SE-EPI DWI, which improves the DWI signal-to-noise ratio (SNR). The resulting diffusion-encoding gradients are necessarily asymmetric about the refocusing pulse and closed-form gradient waveform designs that conform to pulse sequence constraints (ie, the diffusion-encoding gradients must be off during radiofrequency (RF) pulses and the EPI readout, for which the specific timing is dictated by, eg, the field of view, readout bandwidth and spatial resolution), diffusion-encoding gradient waveform constraints (b-value, M$_1$, and M$_2$), and hardware constraints (maximum gradient amplitude and slew rate) are difficult, if not impossible, to determine. Therefore, a mathematical optimization technique is needed.

Convex optimization (CVX) is a proven method for minimizing gradient durations while conforming to pulse sequence and hardware constraints (22,23). The objective of this study was to design and implement a convex optimized diffusion encoding (CODE) framework that can optimize gradient waveforms with any b-value and gradient moment-nulling properties, to simultaneously achieve the shortest possible TE and robustness to bulk motion artifacts:

THEORY

CVX was applied to design diffusion-encoding gradient waveforms that minimize the TE for any b-value with no constraint on the gradient shape or symmetry while conforming to all pulse sequence, diffusion encoding (gradient moment), and hardware constraints, which are defined as follows:

Pulse Sequence Constraints

The diffusion-encoding gradients must be off during both periods of RF activity (excitation and refocusing pulses) and during the EPI readout. Therefore, the diffusion-encoding gradient design must conform to

$$G\left(0 \leq t \leq T_{90(+)}\right) = 0 \qquad [1A]$$

$$G\left(T_{180(-)} \leq t \leq T_{180(+)}\right) = 0 \qquad [1B]$$

$$G(T_{Diff} \leq t \leq TE) = 0 \qquad [1C]$$

where diffusion encoding begins at t = T$_{90(+)}$ (immediately after excitation and EPI correction lines), the refocusing pulse is played when T$_{180(-)} \leq$ t $\leq$ T$_{180(+)}$, and the EPI readout occurs when T$_{Diff} \leq$ t $\leq$ T$_{Diff}$ + T$_{EPI}$ (where T$_{EPI}$ is the EPI readout duration) (Fig. 1a). The duration of the EPI readout gradient necessary to reach the center k-space line is given by the time-to-echo, T$_\varepsilon$, where T$_\varepsilon$ = 0.52•T$_{EPI}$ for full-Fourier imaging.

Gradient Moment Constraints

The optimized diffusion-encoding gradient waveform must have a nulled M_0 and, as required, nulled M_1 or M_1+M_2 at the end of diffusion encoding ($t=T_{Diff}$.) (Fig. 1):

$$M_0 = \int_0^{T_{Diff}} G(t)dt = 0 \qquad [2a]$$

$$M_1 = \int_0^{T_{Diff}} tG(t)dt = 0 \qquad [2b]$$

$$M_2 = \int_0^{T_{Diff}} t^2 G(t)dt = 0 \qquad [2c]$$

The imaging gradients played during the EPI readout have zero net M_0, and negligible M_1, and M_2 at the TE (<1% of typical moments from MONO). Therefore, if they are nulled at $t=T_{Diff}$, they are also effectively nulled at $t=TE$. The moments of the slice select gradient, which are also negligible (<0.5% of typical diffusion-encoding gradient moments for MONO) with respect to the diffusion-encoding gradients, are not considered in this optimization.

Hardware Constraints

The gradient waveform design must adhere to gradient hardware limitations on the maximum gradient amplitude (G_{max}) and slewrate (SR_{max}). This leads to the following constraint terms in the optimization:

$$G(t) \le G_{max} \qquad [3a]$$

$$\dot{G}(t) \le SR_{max} \qquad [3b]$$

Maximizing b-Value

The magnitude of diffusion weighting in a DWI acquisition is characterized by the b-value (b), which is given by

$$b = \gamma^2 \int_0^{T_{Diff}} F(t)^2 dt \qquad [4]$$

where

$$F(t) = \int_0^t G(\tau)d\tau \qquad [5]$$

G(t) is the gradient amplitude as a function of time, T_{Diff} is the time at the end of the diffusion-encoding gradient waveform, and γ is the gyromagnetic ratio of ^{1}H. The time $t=0$ corresponds with the center of the excitation pulse.

The CODE framework begins by determining the maximum b-value for a fixed TE, then subsequently reducing the TE until the maximum b-value is equivalent to the target b-value (b_{target}). However, the b-value (Eq. 4) is a convex function of G(t) (ie, its second variation is positive definite (24)) and therefore does not contain a single

maximum that can be determined with CVX. In addition, Eq. 4 is not a unique function of G(t), which means multiple waveforms can produce the same b-value (eg, +G(t) and −G(t) have the same b-value). Therefore, to facilitate convex optimization, the objective function can be reformulated by defining the function β as follows:

$$\beta = \int_0^{T_{Diff}} F(t)dt \qquad [6]$$

The magnitude of β corresponds directly with the b-value, but it is a concave function of G(t) (ie, its second variation is negative definite (24)); therefore, it contains a maximum that can be determined using CVX. Consequently, the gradient waveform G(t) that produces the maximum β (and thus the maximum b-value) can be determined using the following objective function:

$$G(t) = \underset{G}{\operatorname{argmax}} \beta(G), \qquad [7]$$

subject to the constraints in Eqs. 1-3. G(t) is defined discretely as $t=m \bullet dt$, where dt is the temporal resolution of the optimization, and m is an integer between 1 and T_{Diff}/dt.

Solution Strategy

The time optimal solution is determined by finding the minimum TE for which a gradient waveform exists that is consistent with all constraints (Eqs. 1-3) and has $b_{max} \ge b_{target}$. This problem can be efficiently solved through successive binary searches that divide the TE search space with each iteration of Eq. 7, similar to the method described by Hargreaves et al (22). The search algorithm is shown in a flow chart (Fig. 2) and is provided as a downloadable MATLAB (MathWorks, Natick, Massachusetts) function (http://mrrl.ucla.edu/resources/code-optimization/). Upper and lower limits on TE (TE_U and TE_L) are first defined to initialize the optimization. TE_U is defined by the TE of the nonoptimized sequence with the desired gradient moments (ie, monopolar for $M_0=0$, bipolar for $M_0=M_1=0$, modified bipolar (20) for $M_0=M_1=M_2=0$). TE_L is defined by the TE of an equivalent spin echo sequence (ie, without diffusion-encoding gradients), which has a minimum TE of $2 \bullet (0.5 \bullet T_{180} + T_\varepsilon)$.

METHODS

Diffusion-Encoding Gradient Waveform Design

To evaluate the reduction in TE when using CODE, diffusion-encoding gradient waveforms were designed for a range of b-values (100–1000 s/mm²) and T_ε (10–60 ms), corresponding to approximately 0.5–3.0mm in plane resolution, with full Fourier symmetric k-space coverage, using the following designs: (1) monopolar (MONO, Fig. 1a); (2) CODE with $M_0=0$ (CODE, Fig. 1b); (3) velocity compensated ($M_0=M_1=0$) bipolar (BIPOLAR, Fig. 1c); (4) velocity compensated ($M_0=M_1=0$) CODE (CODE-M_1, Fig. 1d); (5) velocity and acceleration compensated ($M_0=M_1=M_2=0$) modified bipolar (MOCO, Fig. 1e); and
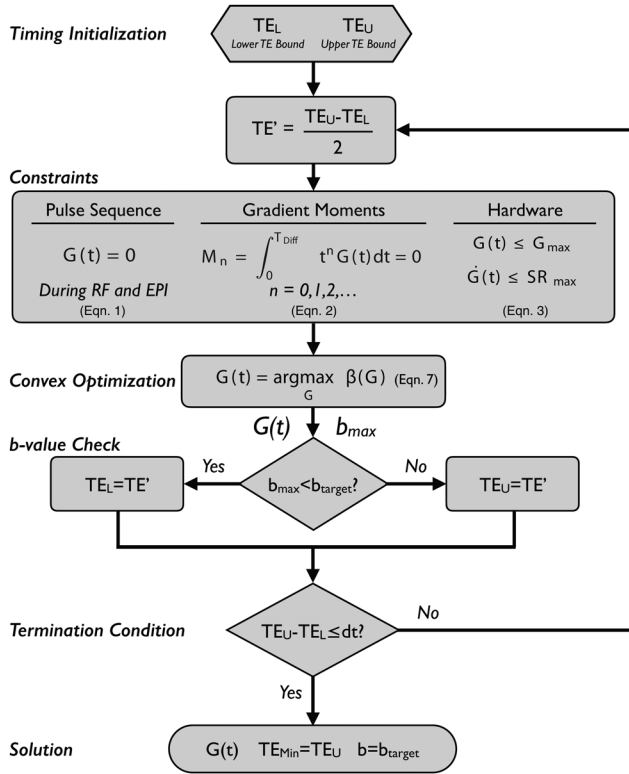
FIG. 2. Flow chart describing the CODE optimization algorithm. The time-optimal solution is determined by finding the minimum TE for which a gradient waveform exists that is consistent with all constraints and can achieve the target b-value (b_{target}). This problem is solved through successive binary searches to divide the TE search space with each call of the convex solver. Upper and lower limits on TE (TE_U and TE_L) are first defined to initiate the optimization. TE_U is defined by the TE of the nonoptimized sequence with the desired gradient moments. TE_L is defined by the TE of an equivalent spin echo sequence (ie, without diffusion-encoding gradients), which has a minimum TE of $2 \cdot (0.5 \cdot T_{180} + T_\varepsilon)$. The function β is defined in Eq. 4 and is directly related to the b-value (ie, maximizing β also maximized b-value), but is compatible with convex optimization.

(6) velocity and acceleration-compensated CODE (CODE-M_1M_2, Fig. 1f).

All diffusion-encoding gradient waveforms were designed for a 3 Tesla (T) MRI scanner (Prisma, Siemens, Erlangen, Germany) with high-performance gradients ($G_{max} = 80$ mT/m and $SR_{max} = 200$ T/m/s). To limit peripheral nerve stimulation during diffusion encoding, the gradient performance was limited to $G_{max} = 74$m T/m and $SR_{max} = 50$ T/m/s. All optimizations were done in MATLAB using the CPLEX linear solver (IBM, Armonk, New York) with the YALMIP toolbox (25); time-step $dt = 100 \mu s$ was used to maintain reasonable computation times (<5 min). Shorter time steps increase the computational demand without significantly reducing echo times.

Concomitant Field Correction

The application of a gradient field leads to the production of concomitant magnetic fields as described by the higher order terms of Maxwell's equations (26–29). Because DWI typically employs large-gradient amplitudes, these fields can have a notable effect and lead to erroneous DWI pixel values, distorted images, and consequently problematic ADC maps. Concomitant fields are not typically an issue in DWI because they are canceled out when diffusion-encoding gradient waveforms are identical on either side of a refocusing pulse. However, because the CODE gradient waveforms are not identical on either side of the refocusing pulse, the concomitant fields must be accounted for. Therefore, a prospective approach that has been used in PC-MRI (30) and DWI (30,31) was implemented in the CODE sequence. Phase variations resulting from concomitant fields were linearly approximated on the scanner for the direction-specific diffusion-encoding gradient waveform and were corrected by adding a gradient magnitude offset to the diffusion-encoding gradient waveform along the x, y, and z axes. Further details on the correction can be found in Ref. (30).

In Vivo Protocols

DWI protocols were designed for neuro ($T_\varepsilon = 27.1$ ms, $T_{90(+)} = 5.8$ ms, $T_{180} = 4.3$ ms), liver ($T_\varepsilon = 26.4$ ms, $T_{90(+)} = 5.3$ ms, $T_{180} = 4.3$ ms), and cardiac ($T_\varepsilon = 25.3$ ms, $T_{90(+)} = 5.4$ ms, $T_{180} = 4.3$ ms) acquisitions with and without CODE. The specific parameters are defined in Table 1. All acquisitions included diffusion encoding along three oblique orthogonal directions. In the cardiac

Table 1
Specific Imaging Parameters Used in the Neuro, Liver, and Cardiac Protocols[a]

	Neuro		Liver			Cardiac		
	MONO	CODE	MONO	BIPOLAR	CODE-M_1	MONO	MOCO	CODE-M_1M_2
TE (ms)	75	64	67	97	72	65	93	76
TR (ms)	5000 ms		1000 ms			1 Heartbeat		
Resolution (mm)	$1.6 \times 1.6 \times 3.0$		$2.0 \times 2.0 \times 7.0$			$1.5 \times 1.5 \times 5$		
FOV (mm)	220×220		300×300			200×160		
BW (Hz/px)	1450		1740			2000		
b (s/mm^2)	0, 1000		0, 500			0, 350		
Fat suppression	None		SPAIR (44)			Water excitation		
Common	Parallel Imaging Acceleration (GRAPPA) (45)) factor 2, full-Fourier k-space sampling							

[a]Interleaved multislice imaging was used in the liver protocols. Reduced FOV imaging was used in the cardiac protocols using phase cycling between the 90° and 180° pulses. Additional fat suppression was achieved in the cardiac protocols using spatially selective saturation bands.

protocols, field of view (FOV) reduction was performed in the phase-encode direction using phase cycling between the excitation and refocusing RF pulses (32).

Concomitant Field Evaluation

To evaluate the performance of the concomitant field correction strategy, DWI were acquired in a uniform water phantom along seven directions (x, y, z, xy, xz, yz, and xyz) using MONO diffusion encoding as a reference for comparison to both CODE-M_1M_2 with and without the concomitant field correction (using the cardiac DWI protocols). Maps from single-direction projections of the ADC were reconstructed independently for each direction, in addition to a composite ADC map (from all directions).

Phantom Validation

All protocols were performed in a polyvinylpyrrolidone diffusion phantom (High Precision Devices, Boulder, Colorado) containing 13 regions with varying diffusivities. The ADC was reconstructed for each protocol, and the mean value was calculated within each of the 13 regions. Mean ADCs obtained with the neuro (MONO and CODE with b = 1000 mm²/s), liver (MONO and CODE-M_1 with b = 500 mm²/s), and cardiac protocols (MONO and CODE-M_1M_2 with b = 350 mm²/s) were compared using linear regression analysis.

In Vivo Acquisitions

MRI examinations were performed on healthy volunteers who provided signed statements of informed consent prior to each MRI exam. All studies were in compliance with the local internal review board, state, and federal guidelines. All imaging was performed on a 3T MRI scanner (Prisma, Siemens, Erlangen, Germany).

Neuro DWI

DWI of the brain were acquired in healthy volunteers (n=10) in a single axial slice with the neuro MONO and CODE protocols. All acquisitions included three discarded TRs to reach steady state, and were repeated 10 times for SNR analysis (scan time: 3 min, 40 s).

ADC maps were reconstructed for each of the 10 repetitions of MONO and CODE using linear least squares. A voxelwise SNR map was generated by dividing the mean ADC at each voxel by the standard deviation (across the 10 repetitions). The global mean SNR was then calculated within the brain for CODE and MONO and compared across the 10 subjects.

Liver DWI

Breath-held liver DWI were acquired in healthy volunteers (n=10) using the MONO, BIPOLAR, and CODE-M_1 liver protocols with three averages. Cardiac triggering was not used. Slice-interleaved imaging was used to acquire four slices per TR and provide coverage of the superior and inferior liver in two breath holds (eight slices). Additional non-diffusion-weighted (b=0) images were also acquired separately with four repetitions (three averages per repetition) for SNR analysis. All acquisitions included three discarded TRs to reach steady state (scan time: 15 s per breath hold).

ADC maps were reconstructed for MONO, BIPOLAR, and CODE-M_1 acquisitions using linear least squares. Four regions of interest (ROIs) were defined manually in homogeneous liver regions (free of vessels) in the lateral left lobe (LL), medial left lobe (ML), superior right lobe (SR), and inferior right lobe (IR). The mean ADC was calculated within each ROI for each acquisition. To identify motion corruption, the mean ADCs in the three superior ROIs (ADC_{LL}, ADC_{ML}, and ADC_{SR}) were compared with that in IR (ADC_{IR}, most inferior and least influenced by cardiac motion).

SNR maps were then calculated from the b=0 images for MONO, BIPOLAR, and CODE-M_1 (voxelwise standard deviation divided by mean signal across repetitions). The mean SNR was calculated within the IR ROI and compared among MONO, BIPOLAR, and CODE-M_1 across the 10 subjects.

Cardiac DWI

Cardiac MRI examinations were performed in healthy volunteers (n=10). First, the timing of end systole (T_{SYS}, the time point with minimum ventricular volume) and early diastole (T_{DIA}, the first time point after rapid filling) were visually determined for each subject using high temporal resolution (20 ms), balanced steady state, free precession (bSSFP) CINE imaging.

Breath-held DWI images were then acquired using the MONO and CODE-M_1M_2 cardiac protocols. Both protocols were acquired with ECG triggering, delayed to the following eight subject-specific cardiac phases: $0.5T_{SYS}$, $0.75T_{SYS}$, T_{SYS}, $T_{SYS}+0.25(T_{DIA}-T_{SYS})$, $T_{SYS}+0.5(T_{DIA}-T_{SYS})$, T_{DIA}, $T_{DIA}+0.25(RR-T_{DIA})$, and $T_{DIA}+0.5(RR-T_{DIA})$, where RR is cardiac cycle duration. Each acquisition included three discarded TRs to reach steady state and three repetitions to improve SNR (scan time: 15 heartbeats or ~15 s).

ADC maps were reconstructed for each cardiac phase for both MONO and CODE-M_1M_2 cDWI using linear least squares. Masks were manually defined to isolate the LV myocardium at each cardiac phase based on the non-diffusion-weighted images. The mean ADC was calculated within the LV for each phase and compared with the diffusivity of free water at 37 °C (3.0×10^{-3} mm²/s, a thermodynamic upper bound for soft-tissue ADC) using a one-sided comparison. Motion-corrupted measurements were identified by voxels in which the reported ADC exceeded 3.0×10^{-3} mm²/s. The percentage of LV voxels with motion corruption was calculated for MONO and CODE-M_1M_2 at each cardiac phase and compared across the 10 volunteers.

An additional cohort of volunteers (n=10) were scanned using MONO, MOCO, and CODE-M_1M_2 at a single systolic phase ($0.5\,T_{SYS}$) for SNR and ADC comparisons between methods. Two acquisitions were obtained for each technique in separate breath holds: (1) the cardiac ADC mapping protocol with three averages, and (2) four repetitions of the non-diffusion-weighted (b=0) images (three averages per repetition). ADC maps were
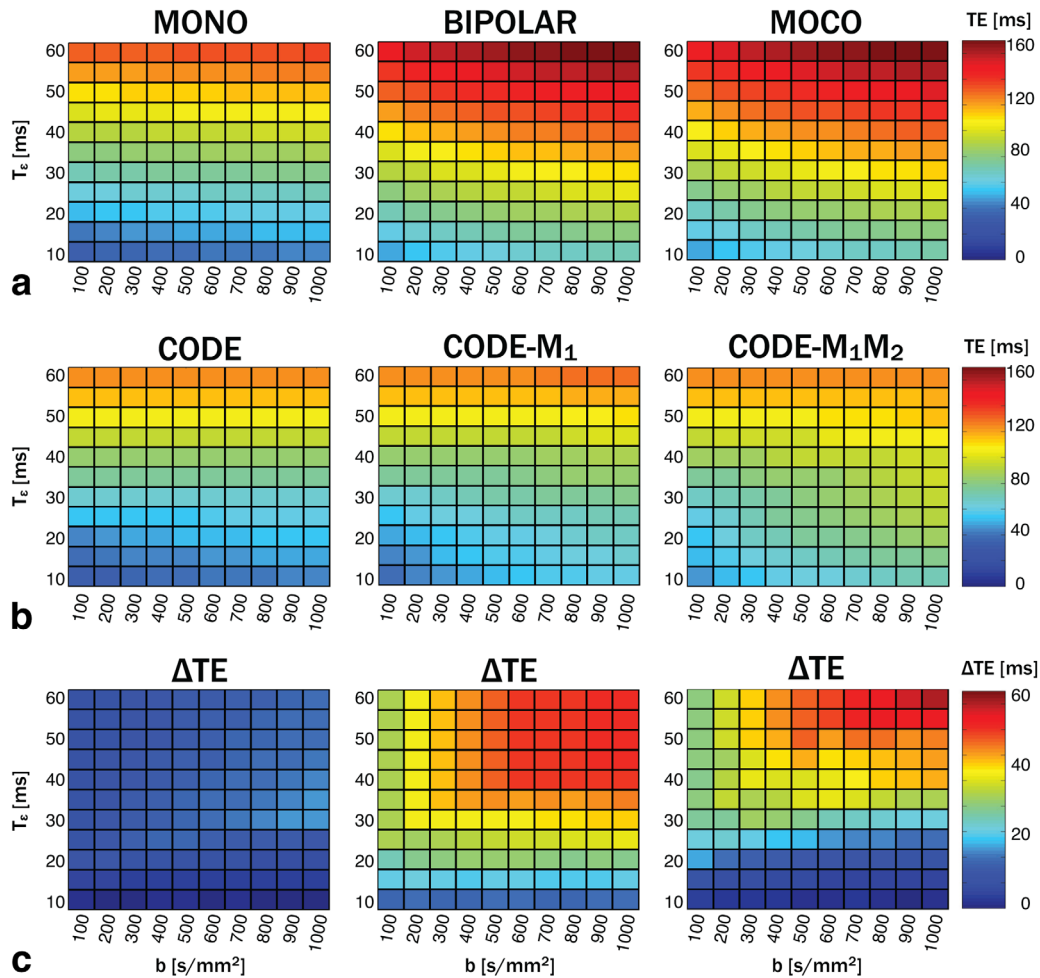
FIG. 3. Minimum TE for a range of b-values and EPI readout times to echo (T_ε) using conventional monopolar (MONO), BIPOLAR, or MOCO diffusion encoding (a), and CODE, CODE-M_1, and CODE-M_1M_2 gradient waveforms (b). TE reduction (ΔTE) achieved using the CODE framework (c). ΔTE was greater for motion-compensated encoding and increased with increasing T_ε.

reconstructed from the DWI sets as described previously. SNR maps were generated from the b=0 images by dividing the mean signal intensity at each voxel by the standard deviation (across the four repetitions). The mean ADC, ADC standard deviation (SD), and mean SNR were then calculated within the septum and compared between MONO, MOCO, and CODE-M_1M_2 across the 10 subjects. Measurements were limited to the septum to remove SNR variations caused by field inhomogeneity in the posterior wall near the lung.

Statistical Analysis

All data were first tested for normality using a skewness and kurtosis test for normality. Variability among groups (eg, between methods or liver ROIs) was then tested using one-way analysis of variance (ANOVA) (for normal distributions) or Kruskal-Wallis (for nonnormal distributions). Variations across cardiac phases were tested using repeated measures ANOVA (normal distributions) or Friedman's test (nonnormal distributions). If ANOVA yielded significant differences ($P < 0.05$), pairwise comparisons were made between groups (eg, MONO versus CODE) using paired t-tests (normal distributions) or

Wilcoxon signed-rank tests (nonnormal distributions) at a 0.05 significance level. Multiple comparisons (ie, between techniques, cardiac phases, and liver ROIs) were evaluated using post hoc Holm-Sidak correction (33).

RESULTS

CODE Optimization

Convex optimization reduced the TE for all diffusion-encoding strategies, ie, CODE, CODE-M_1, and CODE-M_1M_2 across a wide range of b-values and EPI readouts (Fig. 3). The minimum TE for each strategy over a range of b-values and T_ε are plotted in Figure 3. The TE reductions achievable with CODE increased with both longer T_ε (ie, high spatial resolution) and large b-values. Mean TE reductions from CODE, CODE-M_1, and CODE-M_1M_2 were 9.1, 26.5, and 18.4%, respectively, compared with MONO, BIPOLAR, and MOCO. The maximum respective reductions were 17.2, 32.6, and 28.0%. Example waveforms for each encoding strategy are shown in Figure 1 for b-value = 500 s/mm^2 and $T_\varepsilon = 26.4$ ms ($\sim$2x2 mm^2 resolution, equivalent to the liver protocols).

For the neuro protocol ($T_\varepsilon = 27.1$ ms, b = 1000 s/mm^2) the MONO waveform requires TE = 75 ms, whereas
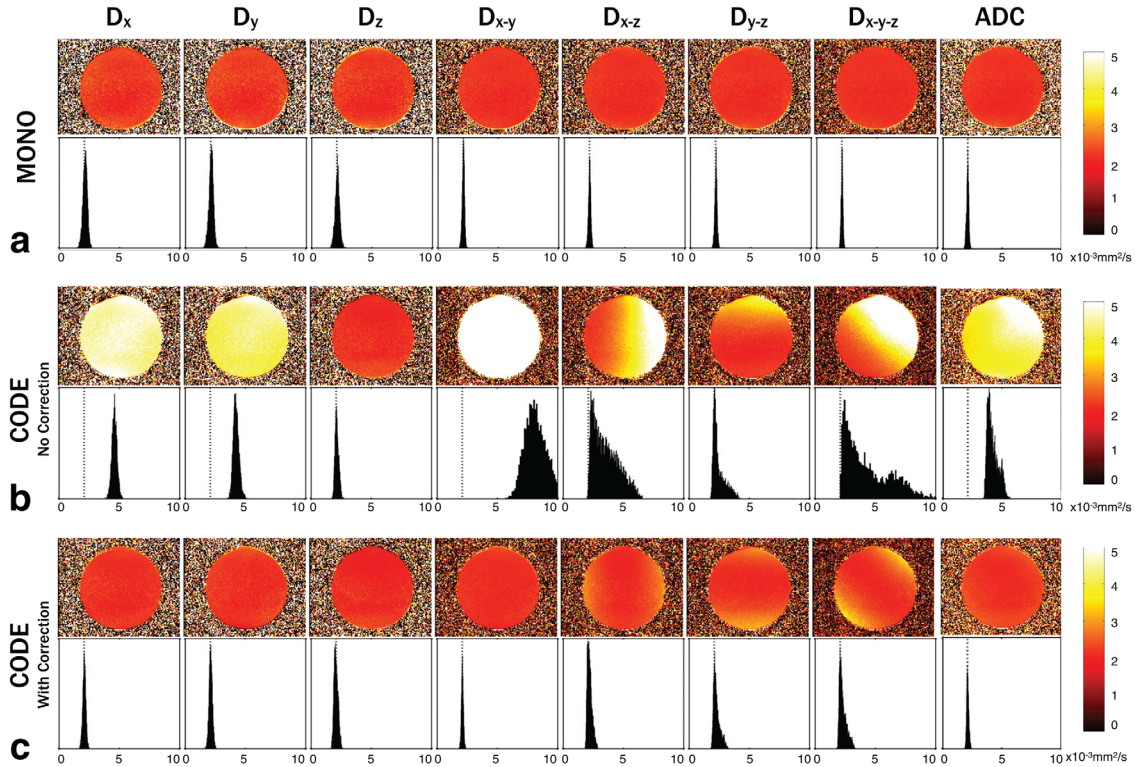
FIG. 4. Measured diffusivity maps and histograms along each gradient direction (D_i) and the final ADC maps (rightmost column) for MONO (a), CODE-M_1M_2 without concomitant field corrections (b), and CODE-M_1M_2 with concomitant field corrections in a uniform water phantom (c). Without the correction, the CODE-M_1M_2 gradients produce large concomitant fields that lead to errors (bias and heterogeneity) in the ADC maps that is also evident in the histograms. The concomitant field correction largely eliminates this effect. The dotted line indicates ADC = 2.1 × 10^{-3} mm^2/s (the "true" value as determined from MONO encoding).

CODE had TE = 67 ms (11% reduction). For the liver protocol (T_ε = 26.4 ms, b = 500 s/mm^2), the M_1-compensated BIPOLAR waveform requires TE = 97 ms, whereas CODE-M_1 had TE = 72 ms (26% reduction). For the cardiac protocol (T_ε = 25.3 ms, b = 350 s/mm^2), the traditional M_1M_2 compensated (MOCO) waveform requires TE = 93 ms, whereas CODE-M_1M_2 had TE = 76 ms (18% reduction).

Concomitant Field Corrections

The effect of the prospective concomitant field correction is shown in Figure 4. With MONO encoding (no concomitant fields, no correction), the ADC projections were spatially homogeneous and the ADC values were distributed tightly about the free diffusivity of water at room temperature ($D_{H20} \approx$ 2.1 × 10^{-3} mm^2/s) for all diffusion-encoding directions. Without the concomitant field correction, CODE-M_1M_2 encoding resulted in a large bias and direction-dependent spatial heterogeneity in the ADC projections. The concomitant field correction significantly reduced the error and spatial variation of the ADC projections for all directions. Mean ADC projections measured across all directions by CODE-M_1M_2 were significantly different from MONO without the correction (4.3 ± 2.2 × 10^{-3} mm^2/s versus 2.1 ± 0.005 × 10^{-3} mm^2/s, P = 0.01), but were not different with the correction (2.1 ± 0.004 × 10^{-3} mm^2/s versus 2.1 ± 0.005 × 10^{-3} mm^2/s, P = N.S.).

Phantom Validation

There was good agreement between MONO and CODE for all three sets of protocols across the range of diffusivities in the diffusion phantom (range: 0.3 × 10^{-3} mm^2/s to 2.1 × 10^{-3} mm^2/s). Regression analysis yielded the following linear fits for each pair of protocols: *Neuro* – ADC$_{CODE}$ = 0.92*ADC$_{MONO}$ + 0.06 × 10^{-3} mm^2/s (R^2 = 0.997), *Liver* – ADC$_{CODE-M1}$ = 0.94*ADC$_{MONO}$ + 0.07 × 10^{-3} mm^2/s (R^2 = 0.99), *Cardiac* – ADC$_{CODE-M1M21}$ = 1.02*ADC$_{MONO}$ + 0.21 × 10^{-3} mm^2/s (R^2 = 0.92).

Neuro DWI

The results from the neuro acquisitions are shown in Figure 5. CODE encoding reduced the TE by 11% as compared with MONO (from 75 to 67 ms), which resulted in ADC maps with higher SNR (Fig. 6c). The mean global SNR of the ADC maps was 35% higher with CODE than MONO (19.5 ± 2.5 versus 14.5 ± 1.9, $P < 0.0001$) across the 10 scanned volunteers.

Liver DWI

Results from the liver acquisitions are shown in Figure 6. MONO encoding resulted in large bulk motion signal dropouts in portions of the liver that are closest to the heart (ie, superior regions and left lobe, Fig. 6a). These signal dropouts lead to large overestimates of the ADC and were eliminated with BIPOLAR and CODE-M_1
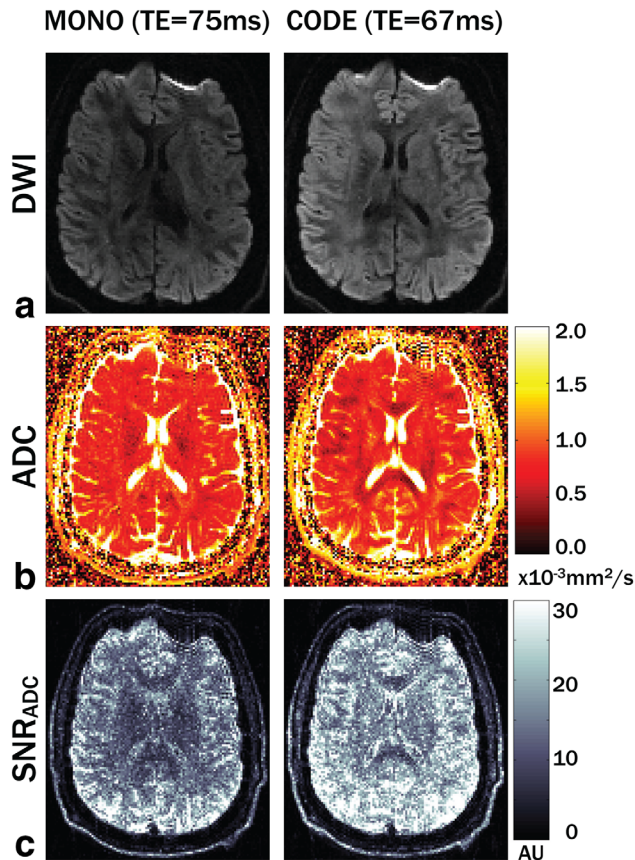
MONO (TE=75ms) CODE (TE=67ms)

FIG. 5. Diffusion-weighted images of the brain from a typical healthy volunteer are shown with $b = 1000$ s/mm^2 using MONO (TE $= 75$ ms) and CODE (TE $= 67$ ms) encoding (a). The 12% TE reduction leads to brighter DWI and qualitatively improved ADC maps (b). The SNR of the ADC maps measured voxelwise from 10 repeated experiments per subject show increased SNR (c). ADC SNR throughout the brain was increased by 35% on average across 10 volunteers with CODE encoding.

encoding (Fig. 6b). Across the 10 volunteers, the mean ADC measured in left-most ROIs (ADC$_{LL}$ and ADC$_{ML}$) were significantly higher than in the most inferior ROI (ie, least influenced by cardiac motion, ADC$_{IR}$) with MONO (Table 2, both $P < 0.004$). There was no significant difference between ADC$_{IR}$ and ADC$_{SR}$ with MONO (Table 2, $P = $ N.S.). Notably, there were no significant differences among the four BIPOLAR or CODE-M$_1$ ROIs (Table 2). With MONO, the maximum difference between mean ADCs across the four ROIs normalized by the mean ADC in the IR (ie, [ADC$_{LL}$-ADC$_{IR}$]/ADC$_{IR}$) was 55%; this decreased to 41% with BIPOLAR and 6% with CODE-M$_1$. The mean ADC was also lower with CODE-M$_1$ than MONO in a pairwise comparison to MONO in three of the four ROIs (ADC$_{LL}$, ADC$_{ML}$, and ADC$_{SR}$, all $P < 0.006$). ADC$_{LL}$ and ADC$_{ML}$ were lower with BIPOLAR than MONO ($P < 0.006$), but there was no significant difference in ADC$_{SR}$. There were no significant differences among the techniques in ADC$_{IR}$.

CODE-M$_1$ and MONO both had significantly higher SNR than BIPOLAR (Fig. 6e) (CODE-M$_1$: 14.9 ± 5.3; MONO: 17.5 ± 6.8 versus BIPOLAR: 8.0 ± 3.1, both

$P < 0.003$). SNR was not significantly different between MONO and CODE-M$_1$.

Cardiac DWI

Results from the cardiac DWI acquisitions are shown in Figures 7 and 8. Qualitatively, Figure 7a demonstrates acceptable DWI when using CODE-M$_1$M$_2$, but unacceptable bulk-motion signal losses when using MONO in most cardiac phases. Mean ADC values were significantly corrupted ($>3.0 \times 10^{-3}$ mm^2/s) for 50% of the cardiac phases with MONO ($P < 0.004$) and 0% of the cardiac phases with CODE-M$_1$M$_2$ ($P = $ N.S.) (Fig. 7b). CODE-M$_1$M$_2$ resulted in significantly lower mean ADCs ($1.9 \pm 0.3 \times 10^{-3}$ mm^2/s versus $3.8 \pm 0.6 \times 10^{-3}$ mm^2/s, $P < 0.007$) and fewer motion-corrupted voxels (14% versus 67%, $P < 0.0006$) than MONO in 100% of cardiac phases (Figs. 7b and 7c).

Figure 8a demonstrates the improved motion robustness of both MOCO and CODE-M$_1$M$_2$ compared with MONO and also the SNR gains of CODE-M$_1$M$_2$ compared with MOCO. Mean ADCs were not different between CODE-M$_1$M$_2$ and MOCO ($1.5 \times 10^{-3} \pm 0.2$ mm^2/s versus $1.4 \times 10^{-3} \pm 0.6$ mm^2/s, $P = $ N.S.) (Fig 8b), but CODE-M$_1$M$_2$ had significantly lower ADC variance than MOCO (mean SD $= 0.7 \times 10^{-3} \pm 0.3$ versus $0.9 \times 10^{-3} \pm 0.3$, $P < 0.002$) (Fig 8c) and significantly higher SNR (9.1 ± 3.9 versus 7.0 ± 2.6, $P < 0.02$) (Fig 8d). MONO had significantly higher SNR (mean SNR $= 11.0 \pm 5.9$) than MOCO (mean SNR $= 7.0 \pm 2.6$, $P < 0.002$), and slightly higher SNR than CODE-M$_1$M$_2$ (mean SNR $= 9.1 \pm 3.9$, $P = $ N.S.), but reported corrupted ADC values that were significantly higher than CODE-M$_1$M$_2$ and MOCO (mean ADC $= 4.4 \times 10^{-3} \pm 1.6$ mm^2/s, $P < 1 \times 10^{-5}$ for MOCO and CODE-M$_1$M$_2$) (Fig 8b).

DISCUSSION

In this study, time-optimal, bulk motion–compensated DWI with CODE gradient waveforms was described, implemented, and evaluated in vivo on a clinical scanner. CODE reduced the TE for all combinations of b-value and T$_\varepsilon$ (Fig. 2), and the largest reductions were seen for combinations of longer T$_\varepsilon$ (higher spatial resolution) and larger b-values. The benefit of CODE is greatest for high-resolution imaging (long T$_\varepsilon$) and is likely to be minimal in applications requiring coarse spatial resolution. Similarly, applications using low b-values may not benefit as much as applications that require large b-values, such as q-space (34) or diffusion spectrum (35) imaging.

TEs can also be reduced using partial Fourier acquisitions that asymmetrically sample k-space and shorten T$_\varepsilon$. Reducing T$_\varepsilon$ decreases the TE reduction benefit from CODE (Fig. 3). However, partial Fourier can lead to signal dropouts resulting from bulk vibrations or rotations (36,37). CODE can achieve TE reductions similar to partial Fourier methods without these adverse effects and while acquiring more k-space lines for improved SNR. For example, neuro CODE permitted full-Fourier with a negligible TE increase compared with MONO with 7/8 PF (67 ms versus 63 ms), liver CODE-M$_1$ with full-Fourier had a shorter TE than BIPOLAR with 7/8 PF (72
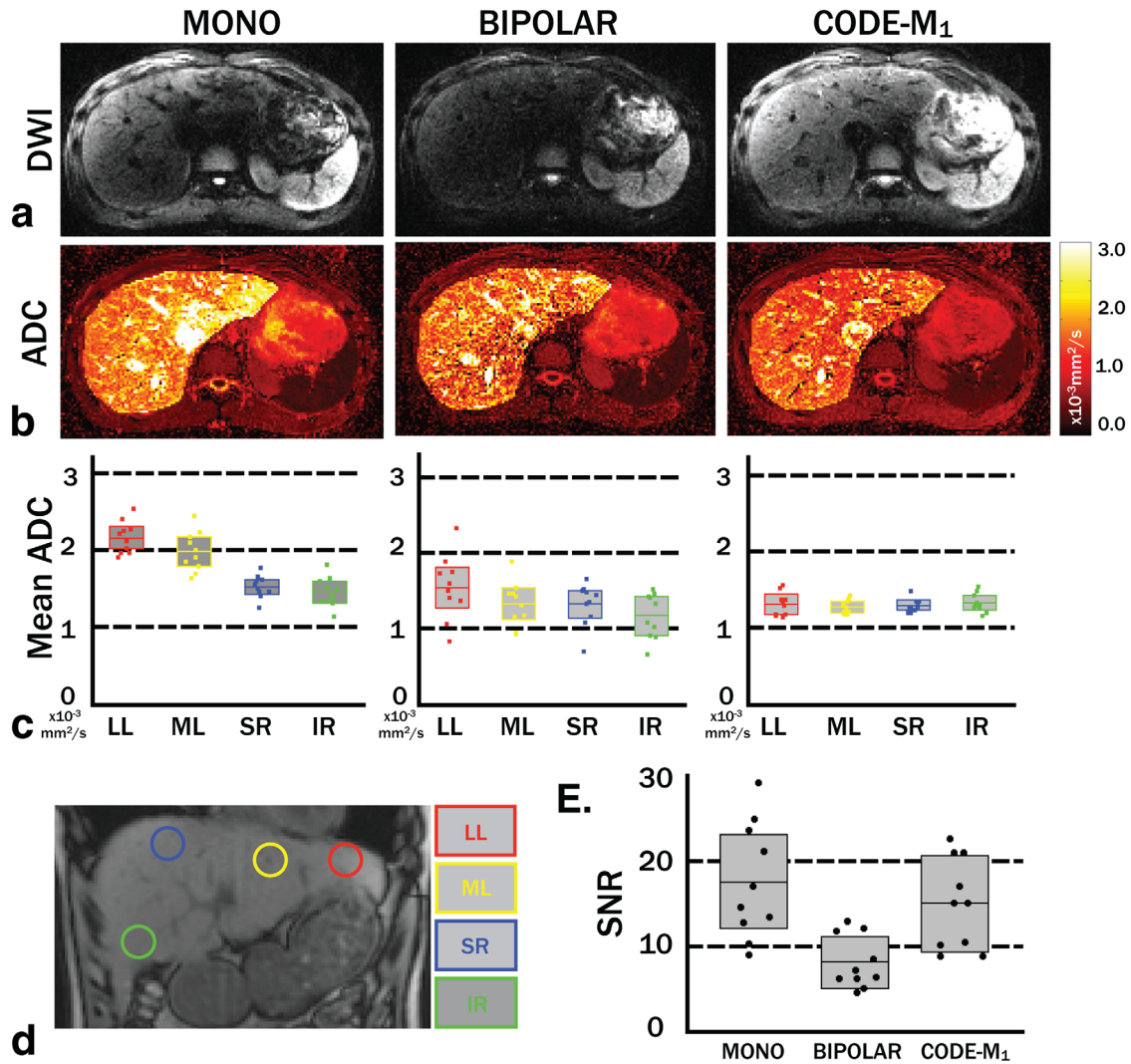
FIG. 6. Axial diffusion-weighted images of the liver from a typical healthy volunteer are shown with $b = 500$ s/mm^2 using MONO, BIPO-LAR, and CODE-M$_1$ (a). Signal dropouts caused by physiological motion lead to elevated ADC maps, but are largely eliminated with CODE-M$_1$ (b). Mean $\pm$ 95% CI ADC values within the four ROIs across 10 volunteers (c). The MONO ADC values are higher close to the heart (LL, left lobe; ML, middle lobe), where cardiac-induced bulk motion is greatest. CODE-M$_1$ encoding leads to more spatially homogeneous ADC maps. Approximate regions chosen for the four ROIs are shown in the coronal view (d). Mean $\pm$ 95% CI SNR values within the IR ROI across the 10 volunteers for MONO, BIPOLAR, and CODE-M$_1$ encoding (e). CODE-M$_1$ had greater SNR than BIPO-LAR, while maintaining motion robustness.

ms versus 84 ms), and cardiac CODE-M$_1$M$_2$ with full-Fourier had a shorter TE than MOCO with 7/8 PF (76 ms versus 81 ms). Note that all comparisons assumed two-fold parallel imaging acceleration, which already approximately halves T$_{EPI}$ and T$_\varepsilon$.

Table 2
Mean ADC Values Measured in the Four Liver ROIs

	ADC$_{LL}$	ADC$_{ML}$	ADC$_{SR}$	ADC$_{IR}$
MONO	2.1 ± 0.3^a	2.0 ± 0.5^a	1.5 ± 0.3	1.5 ± 0.3
BIPOLAR	1.5 ± 0.6^b	1.2 ± 0.4^b	1.3 ± 0.4	1.2 ± 0.5
CODE-M$_1$	1.3 ± 0.2^b	1.2 ± 0.1^b	1.3 ± 0.2^b	1.3 ± 0.2

LL, left lobe; ML, middle lobe; SR, superior right; IR, inferior right.
[a]Indicates mean ADCs that are significantly different from ADC$_{IR}$ ($P < 0.003$).
[b]Indicates that mean ADCs are significantly different from MONO.

CODE gradient waveforms were designed to be optimal along any gradient direction and can thus be applied to diffusion tensor imaging (DTI) or higher order q-space sampling. However, because the diffusion-encoding direction affects the available gradient amplitude (G$_{max}$ effectively increases when more gradient axes are active simultaneously), the directions to be sampled must be accounted for in the optimization.

Although the prospective concomitant field correction significantly reduced image artifacts, some residual errors could still be seen along some diffusion-encoding directions, as evidenced by overestimates of diffusivity near the phantom edges (eg, *x-z, y-z, x-y-z* in Fig. 3). These are likely caused by the linear field approximation made in the correction. However, because these errors varied spatially with different diffusion-encoding directions, the final ADC maps had minimal errors throughout
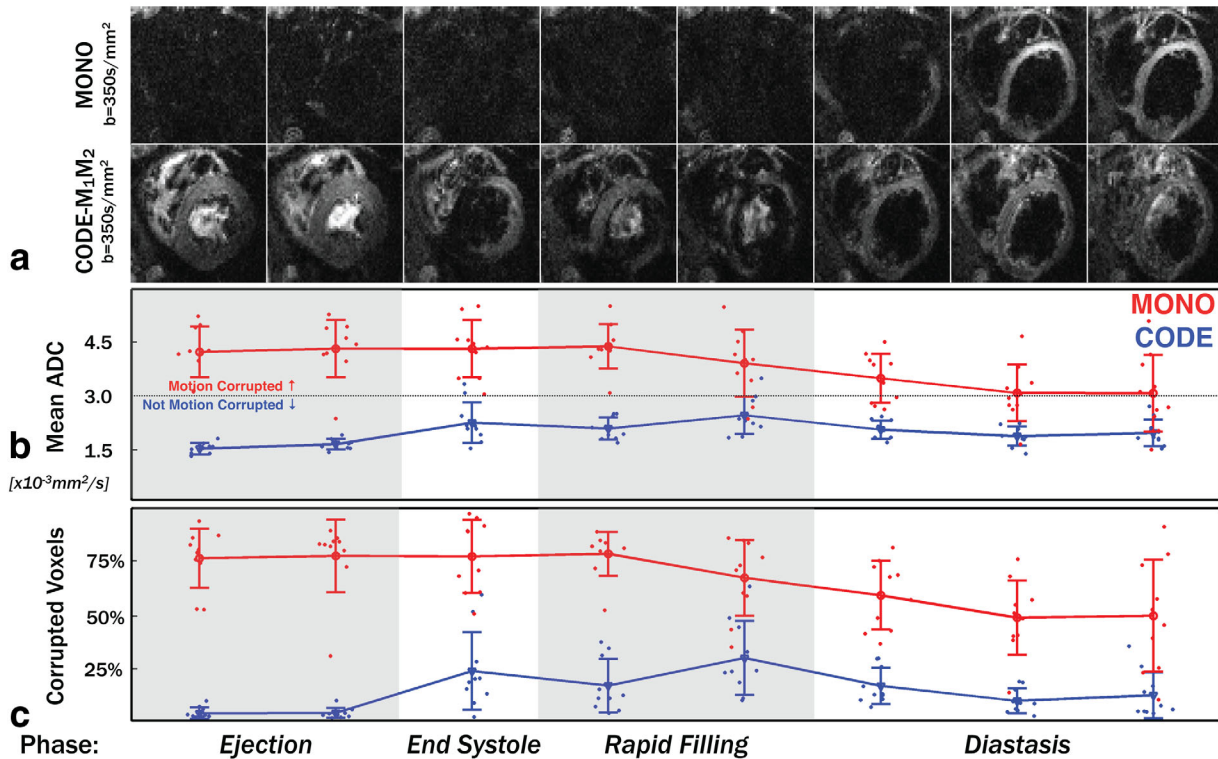
FIG. 7. Diffusion-weighted images are shown from a typical healthy volunteer acquired at eight different cardiac phases with MONO and CODE-M_1M_2 (a). Motion corruption in MONO is highly subject-dependent and varies greatly with cardiac phase. Mean $\pm$ SD LV ADC values (b) and percentage$\pm$SD (c) of motion-corrupted (ADC $> 3.0 \times 10^{-3}$ mm^2/s) LV voxels for MONO and CODE-M_1M_2 across the 10 volunteers. CODE-M_1M_2 is much less sensitive to bulk motion and is not as dependent on precise sequence timing as shown by both the lower ADC measurements (b) and lower percentage of motion-corrupted voxels (b) for all cardiac phases.

the FOV. Further investigation into more sophisticated corrections is warranted and may be necessary for use in DTI.

No apparent eddy current distortions were observed in any of the CODE DWI compared with the non-diffusion-weighted images or with MONO, BIPOLAR, or MOCO encoding. There were also no issues associated with gradient heating or system instability from any of the CODE sequences.

Although the phantom experiments showed good agreement between CODE and MONO in all protocols, CODE-M_1M_2 showed a slight positive ADC bias and increased variability as compared with MONO. One possible explanation is the lower SNR of this particular protocol caused by its high spatial resolution (1.5 mm in-plane) and relatively long TE (TE = 75 ms). Previous reports have shown through simulation that low SNR imaging can lead to overestimates of ADC (38).

All gradient optimizations were performed with the slew rate constrained to $\leq$50 T/m/s, which is significantly less than the 200 T/m/s capability of the gradient system. This is a conservative bound that is software-imposed on all diffusion-encoding gradients to avoid peripheral nerve stimulation (PNS). TEs can be further reduced if this constraint is relaxed, which can likely be done safely. Recent work has shown that a more sophisticated PNS model based on nerve response functions can be applied to safely shorten gradient waveforms (39).

Future work will include applying a similar approach to the CODE framework.

The neuro scans showed that CODE can improve the SNR of ADC maps by reducing TE compared with monopolar encoding at the same b-value. Neuro DWI often uses high spatial resolutions and large b-values (2000 s/mm^2 or higher), which limit SNR. This necessitates many signal averages and long scan times. The shortened TEs permitted by CODE can reduce the number of averages needed for acceptable SNR. Note that while only single slice imaging was performed, CODE is fully compatible with two-dimensional multislice imaging.

In vivo liver (Fig. 6) and cardiac (Figs. 7 and 8) scans in healthy volunteers demonstrated the value of bulk motion–compensated CODE. The results of this study echo previous reports of M_1M_2-nulled DWI in the heart by Nguyen et al (40), Welsh et al (21), and Stoeck et al (20), as well as M_1-nulled DWI in the liver by Ozaki et al (18). The CODE framework is specifically designed for SE-EPI DWI and needs further evaluation to identify any advantages for diffusion preparation–based sequences. For example, 3D segmented bSSFP with diffusion preparation (40) has a potential image quality advantage over SE-EPI, but also has lower acquisition efficiency and a long diffusion preparation time.

In the liver, CODE-M_1 resulted in lower ADC values than MONO in all regions, even in ROIs distal from the
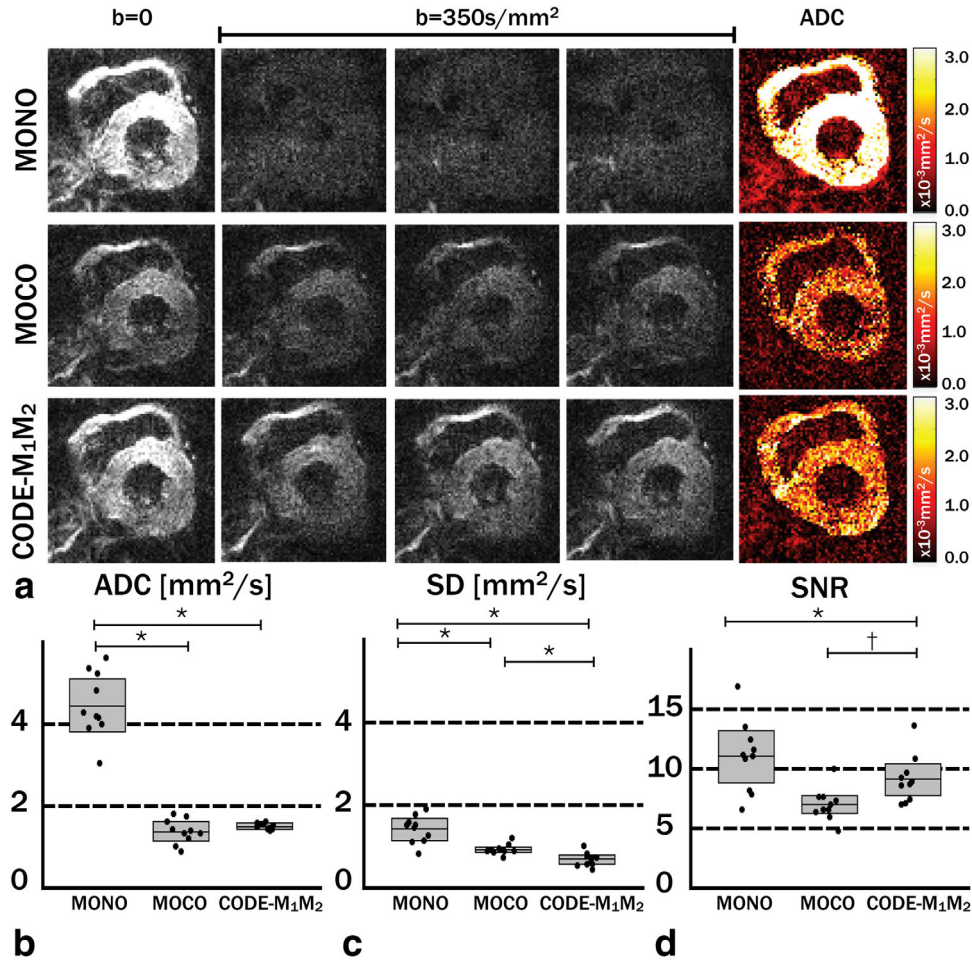
FIG. 8. Diffusion-weighted images and ADC maps are shown from a typical healthy volunteer acquired at a single systolic cardiac phase with MONO, MOCO, and CODE-M_1M_2 (a). MONO led to bulk motion–corrupted DWI and subsequently elevated ADC maps, whereas MOCO and CODE-M_1M_2 led to uncorrupted DWI and physiologically meaningful ADC values. Mean septal ADC values were consistent between MOCO and CODE-M_1M_2, but much higher with MONO (b). CODE-M_1M_2 had less variability in mean ADC. Standard deviations (SD) of the ADC within the septum were lower with CODE-M_1M_2 than MONO or MOCO (c). SNR of the b=0 images was highest with MONO, but DWI were heavily corrupted (d). CODE-M_1M_2 had higher SNR than MOCO, while maintaining bulk motion robustness (*$P<0.002$ †$P<0.02$).

heart and ostensibly free of bulk motion (though not significantly different in the most distal ROI). BIPOLAR reported lower ADC values in all four regions (with significant differences in two of the four). Note too that the CODE-M_1 and MONO ADC measurements were in agreement in the phantom. This discrepancy is likely the result of the perfusion sensitivity in MONO acquisitions that is reduced with CODE-M_1 and BIPOLAR. The motion of perfusing blood within liver tissue contributes to the diffusion-encoding signal decay with MONO, leading to overestimates of ADC. This effect is reduced in CODE-M_1 and BIPOLAR, and is absent as long as blood velocities are constant during diffusion encoding. All ADC reconstructions assumed a single compartment diffusion model and thus could not distinguish this effect.

The present work leverages state-of-the-art gradient hardware that can achieve high gradient amplitudes ($G_{max}=80$ mT/m) and significantly shorten diffusion-encoding gradient waveforms. This reduces the TE and improves bulk motion robustness (reducing the diffusion-encoding footprint) as compared with more commonly available systems (typically $G_{max}=40$ mT/m) (41,42). The benefit of similar maximum gradient amplitude performance for cardiac DWI has been previously demonstrated at 1.5 T (20,43). Although CODE can be used with any gradient hardware and will always reduce TEs compared with symmetric encoding, all TEs will be lengthened significantly when using lower gradient amplitudes and/or lower slew rates. In these cases, moment-nulled diffusion encoding may limit SNR or extend the diffusion-encoding intervals beyond a point that is practical for clinical use. In fact, acceptable image quality with M_1M_2-nulled SE-EPI DWI in the heart has not been demonstrated with $G_{max}=40$ mT/m. Non-motion-compensated CODE (only M_0 nulled) can still be used in this case to minimize the temporal footprint of diffusion encoding. In fact, in some conditions (eg, long T_e), CODE converges to the single-sided bipolar waveform (Fig. 1b), which is designed to be a bulk motion management technique (43).

All CODE gradient waveform design work was performed using MATLAB (2013A) running on a MacBook

Pro (2.3 Ghz Core i7 with 16 GB RAM, Apple, Cupertino, California) and took between 2 and 5 min. This can likely be shortened by converting the optimization software to a faster language and by using a faster computer. However, it remains to be shown that the optimization can be fast enough to be performed during routine clinical exams. In this case, a database of waveforms previously optimized to a wide range of b-values and imaging constraints can be generated and readily accessed on the scanner.

CONCLUSIONS

CODE DWI reduced TEs for DWI with and without motion compensation compared with conventional encoding waveforms. Implementation on a clinical scanner in healthy volunteers demonstrated that CODE improved the SNR of ADC maps in DWI of the brain, whereas CODE-M_1 and CODE-M_1M_2 improved the bulk motion robustness of DWI and ADC maps in the liver and heart with shorter TEs and consequently higher SNR than existing methods.

ACKNOWLEDGMENTS

REFERENCES

1. Wu MT, Su MY, Huang YL, Chiou KR, Yang P, Pan HB, Reese TG, Wedeen VJ, Tseng WY. Sequential changes of myocardial microstructure in patients postmyocardial infarction by diffusion-tensor cardiac MR: correlation with left ventricular structure and function. Circ Cardiovasc Imaging 2009;2(1):32–40, 6 p following.

2. Pop M, Ghugre NR, Ramanan V, Morikawa L, Stanisz G, Dick AJ, Wright GA. Quantification of fibrosis in infarcted swine hearts by ex vivo late gadolinium-enhancement and diffusion-weighted MRI methods. Phys Med Biol 2013;58(15):5009–5028.

3. Potet J, Rahmouni A, Mayer J, Vignaud A, Lim P, Luciani A, Dubois-Randé JL, Kobeiter H, Deux JF. Detection of myocardial edema with low-b-value diffusion-weighted echo-planar imaging sequence in patients with acute myocarditis. Radiology 2013;269(2):362–369.

4. Naganawa S, Kawai H, Fukatsu H, Sakurai Y, Aoki I, Miura S, Kanazawa H, Ishigaki T. Diffusion-weighted imaging of the liver: technical challenges and prospects for the future. Magn Reson Med Sci 2005;4(4):175–186.

5. Demir OI, Obuz F, Sagol O, Dicle O. Contribution of diffusion-weighted MRI to the differential diagnosis of hepatic masses. Diagn Interv Radiol 2007;13(2):81–86.

6. Bruegel M, Holzapfel K, Gaa J, Woertler K, Waldt S, Kiefer B, Stemmer A, Ganter C, Rummeny EJ. Characterization of focal liver lesions by ADC measurements using a respiratory triggered diffusion-weighted single-shot echo-planar MR imaging technique. Eur Radiol 2008;18(3):477–485.

7. Gourtsoyianni S, Papanikolaou N, Yarmenitis S, Maris T, Karantanas A, Gourtsoyiannis N. Respiratory gated diffusion-weighted imaging of the liver: value of apparent diffusion coefficient measurements in the differentiation between most commonly encountered benign and malignant focal liver lesions. Eur Radiol 2008;18(3):486–492.

8. Norris DG. Implications of bulk motion for diffusion-weighted imaging experiments: effects, mechanisms, and solutions. J Magn Reson Imaging 2001;13(4):486–495.

9. Gamper U, Boesiger P, Kozerke S. Diffusion imaging of the in vivo heart using spin echoes—considerations on bulk motion sensitivity. Magn Reson Med 2007;57(2):331–337.

10. Kwee TC, Takahara T, Niwa T, Ivancevic MK, Herigault G, Van Cauteren M, Luijten PR. Influence of cardiac motion on diffusion-weighted magnetic resonance imaging of the liver. MAGMA 2009; 22(5):319–325.

11. Pai VM, Rapacchi S, Kellman P, Croisille P, Wen H. PCATMIP: enhancing signal intensity in diffusion-weighted magnetic resonance imaging. Magn Reson Med 2011;65(6):1611–1619.

12. Rapacchi S, Wen H, Viallon M, Grenier D, Kellman P, Croisille P, Pai VM. Low b-value diffusion-weighted cardiac magnetic resonance imaging: initial results in humans using an optimal time-window imaging approach. Invest Radiol 2011;46(12):751–758.

13. Murtz P, Flacke S, Traber F, van den Brink JS, #Gieseke J, Schild HH. Abdomen: diffusion-weighted MR imaging with pulse-triggered single-shot sequences. Radiology 2002;224(1):258–264.

14. Kwee TC, Takahara T, Koh DM, Nievelstein RA, Luijten PR. Comparison and reproducibility of ADC measurements in breathhold, respiratory triggered, and free-breathing diffusion-weighted MR imaging of the liver. J Magn Reson Imaging 2008;28(5):1141–1148.

15. Chen X, Qin L, Pan D, Huang Y, Yan L, Wang G, Liu Y, Liang C, Liu Z. Liver diffusion-weighted MR imaging: reproducibility comparison of ADC measurements obtained with multiple breath-hold, free-breathing, respiratory-triggered, and navigator-triggered techniques. Radiology 2014;271(1):113–125.

16. Edelman RR, Gaa J, Wedeen VJ, Loh E, Hare JM, Prasad P, Li W. In vivo measurement of water diffusion in the human heart. Magn Reson Med 1994;32(3):423–428.

17. Kwee TC, Takahara T, Ochiai R, Nievelstein RA, Luijten PR. Diffusion-weighted whole-body imaging with background body signal suppression (DWIBS): features and potential applications in oncology. Eur Radiol 2008;18(9):1937–1952.

18. Ozaki M, Inoue Y, Miyati T, Hata H, Mizukami S, Komi S, Matsunaga K, Woodhams R. Motion artifact reduction of diffusion-weighted MRI of the liver: use of velocity-compensated diffusion gradients combined with tetrahedral gradients. J Magn Reson Imaging 2013;37(1):172–178.

19. Nguyen C, Fan Z, Sharif B, He Y, Dharmakumar R, Berman DS, Debiao L. In vivo three-dimensional high resolution cardiac diffusion-weighted MRI: a motion compensated diffusion-prepared balanced steady-state free precession approach. Magn Reson Med 2014;16(Suppl 1):O83.

20. Stoeck CT, von Deuster C, Genet M, Atkinson D, Kozerke S. Second-order motion-compensated spin echo diffusion tensor imaging of the human heart. Magn Reson Med 2015;17(Suppl 1):P81.

21. Welsh C, Di Bella E, Hsu E. Higher-order motion-compensation for in vivo cardiac diffusion tensor imaging in rats. IEEE Trans Med Imaging 2015;34(9):1843–1853.

22. Hargreaves BA, Nishimura DG, Conolly SM. Time-optimal multidimensional gradient waveform design for rapid imaging. Magn Reson Med 2004;51(1):81–92.

23. Middione MJ, Wu HH, Ennis DB. Convex gradient optimization for increased spatiotemporal resolution and improved accuracy in phase contrast MRI. Magn Reson Med 2014;72(6):1552–1564.

24. Gel'fand IM, Fomin SV. Calculus of Variations, Rev. English Ed. Englewood Cliffs, NJ: Prentice-Hall; 1963.

25. Lofberg J. Automatic robust convex programming. Optim Methods Softw 2012;27(1):115–129.

26. Zhou XJ, Du YP, Bernstein MA, Reynolds HG, Maier JK, Polzin JA. Concomitant magnetic-field-induced artifacts in axial echo planar imaging. Magn Reson Med 1998;39(4):596–605.

27. Zhou XJ, Tan SG, Bernstein MA. Artifacts induced by concomitant magnetic field in fast spin-echo imaging. Magn Reson Med 1998; 40(4):582–591.

28. King KF, Ganin A, Zhou XJ, Bernstein MA. Concomitant gradient field effects in spiral scans. Magn Reson Med 1999;41(1):103–112.

29. Sica CT, Meyer CH. Concomitant gradient field effects in balanced steady-state free precession. Magn Reson Med 2007;57(4):721–730.

30. Meier C, Zwanger M, Feiweier T, Porter D. Concomitant field terms for asymmetric gradient coils: consequences for diffusion, flow, and echo-planar imaging. Magn Reson Med 2008;60(1):128–134.

31. Baron CA, Lebel RM, Wilman AH, Beaulieu C. The effect of concomitant gradient fields on diffusion tensor imaging. Magn Reson Med 2012;68(4):1190–1201.

32. Feinberg DA, Hoenninger JC, Crooks LE, Kaufman L, Watts JC, Arakawa M. Inner volume MR imaging: technical concepts and their application. Radiology 1985;156(3):743–747.

33. Holm S. A simple sequentially rejective multiple test procedure. Scand J Stat 1979:65–70.

34. Yeh FC, Wedeen VJ, Tseng WY. Generalized q-sampling imaging. IEEE Trans Med Imaging 2010;29(9):1626–1635.

35. Wedeen VJ, Hagmann P, Tseng WY, Reese TG, Weisskoff RM. Mapping complex tissue architecture with diffusion spectrum magnetic resonance imaging. Magn Reson Med 2005;54(6):1377–1386.

36. Storey P, Frigo FJ, Hinks RS, Mock BJ, Collick BD, Baker N, Marmurek J, Graham SJ. Partial k-space reconstruction in single-shot diffusion-weighted echo-planar imaging. Magn Reson Med 2007; 57(3):614–619.

37. Wedeen VJ, Weisskoff RM, Poncelet BP. MRI signal void due to inplane motion is all-or-none. Magn Reson Med 1994;32(1): 116–120.

38. Gahm JK, Kindlmann G, Ennis DB. The effects of noise over the complete space of diffusion tensor shape. Med Image Anal 2014;18(1): 197–210.

39. Schulte RF, Noeske R. Peripheral nerve stimulation-optimal gradient waveform design. Magn Reson Med 2015;74(2):518–522.

40. Nguyen C, Fan Z, Sharif B, He Y, Dharmakumar R, Berman DS, Debiao Li. In vivo three-dimensional high resolution cardiac diffusion-weighted MRI: a motion compensated diffusion-prepared balanced steady-state free precession approach. Magn Reson Med 2013;72(5):1257–1267.

41. Aliotta E, Rapacchi S, Hu P, Ennis D. Increased maximum gradient amplitude improves robustness of spin-echo cardiac diffusion-weighted MRI. J Cardiovasc Magn Reson 2015; 17(Suppl 1):P388.

42. Aliotta E, Rapacchi S, Hu P, Ennis D. In Vivo Spin Echo EPI Cardiac Diffusion Tensor MRI Using Ultra-High Gradient Amplitudes. Proceedings of the 23rd Annual Meeting of ISMRM, Toronto, Canada, 2015. Abstract 2639.

43. Freidlin RZ, Kakareka JW, Pohida TJ, Komlosh ME, Basser PJ. A spin echo sequence with a single-sided bipolar diffusion gradient pulse to obtain snapshot diffusion weighted images in moving media. J Magn Reson 2012;221:24–31.

44. Lauenstein TC, Sharma P, Hughes T, Heberlein K, Tudorascu D, Martin DR. Evaluation of optimized inversion-recovery fat-suppression techniques for T2-weighted abdominal MR imaging. J Magn Reson Imaging 2008;27(6):1448–1454.

45. Griswold MA, Jakob PM, Heidemann RM, Nittka M, Jellus V, Wang J, Kiefer B, Haase A. Generalized autocalibrating partially parallel acquisitions (GRAPPA). Magn Reson Med 2002;47(6):1202–1210.